Journal of
Materials Chemistry C

PAPER

View Article Online
View Journal | View Issue

Cite this: *J. Mater. Chem. C*, 2024, **12**, 15058

Symmetry-informed design of magnetoelectric coupling in the manganite perovskite $CeBaMn_2O_6$†

Struan Simpson,[a] Cameron A. M. Scott,[b] Fernando Pomiro,[a] Jeremiah P. Tidey,[a] Urmimala Dey,[b] Fabio Orlandi,[c] Pascal Manuel,[c] Martin R. Lees,[d] Zih-Mei Hong,[efg] Wei-tin Chen,[efh] Nicholas C. Bristowe[b] and Mark S. Senn*[a]

Received 28th June 2024,
Accepted 22nd August 2024

DOI: 10.1039/d4tc02743d

rsc.li/materials-c

Magnetoelectric multiferroics hold great promise for the development of new sustainable memory devices. However, practical applications of many existing multiferroic materials are infeasible due to the weak nature of the coupling between the magnetic and electrical orderings, meaning new magnetoelectric multiferroics featuring intrinsic coupling between their component orderings are sought instead. Here, we apply a symmetry-informed design approach to identify and realize the new manganite perovskite $CeBaMn_2O_6$ in which magnetoelectric coupling can be achieved *via* an intermediary non-polar structural distortion. Through first-principles calculations, we demonstrate that our chosen prototype system contains the required ingredients to achieve the desired magnetoelectric coupling. Using high-pressure/high-temperature synthesis conditions, we have been able to synthesize the $CeBaMn_2O_6$ perovskite system for the first time. Our subsequent neutron and electron diffraction measurements reveal that the desired symmetry-breaking ingredients exist in this system on a nanoscopic length scale, enabling magnetoelectric nanoregions to emerge within the material. Through this work, we showcase the potential of the new $CeBaMn_2O_6$ perovskite material as a promising system in which to realize strong magnetoelectric coupling, highlighting the potential of our symmetry-informed design approach in the pursuit of new magnetoelectric multiferroics for next-generation memory devices.

Introduction

The development of energy-efficient memory devices is of crucial technological importance if the world is to achieve its sustainability goals. Ferroelectric memories (FeRAMs) offer promise in this regard owing to their fast access speeds and high storage densities, but their destructive read operations limit the read/write endurance of the storage media. Ferromagnetic memories (MRAMs) offer non-destructive reading *via* the application of magnetoresistive currents, but they are limited by the large energy demands associated with write operations. Multiferroic memories, with ordered electric and magnetic dipoles, combine the advantages of both approaches by allowing data to be written electrically but read magnetically, thus offering dramatically improved device endurance and energy efficiency compared to existing data storage technologies.

Despite their transformative potential in device applications, multiferroic materials with commercially applicable transition temperatures remain rare. For the intensively studied field of perovskite multiferroics, this is largely due to the incompatibility of producing a ferroelectric distortion on a magnetic cation[1] as the presence of empty metal d orbitals is required to stabilize the ferroelectric distortion *via* hybridization with the O 2p electrons.[2] One way to circumvent this is to introduce alternative sources of ferroelectricity such as stereochemically active lone pairs into the

---

[a] *Department of Chemistry, University of Warwick, Gibbet Hill, Coventry, CV4 7AL, UK. E-mail: m.senn@warwick.ac.uk*

[b] *Centre for Materials Physics, Durham University, South Road, Durham, DH1 3LE, UK*

[c] *ISIS Facility, STFC Rutherford Appleton Laboratory, Harwell Science and Innovation Campus, Oxon OX11 0QX, UK*

[d] *Department of Physics, University of Warwick, Gibbet Hill, Coventry, CV4 7AL, UK*

[e] *Center for Condensed Matter Sciences, National Taiwan University, Taipei 106319, Taiwan*

[f] *Center of Atomic Initiative for New Materials, National Taiwan University, Taipei 106319, Taiwan*

[g] *Department of Chemistry, Fu-Jen Catholic University, New Taipei 24205, Taiwan*

[h] *Taiwan Consortium of Emergent Crystalline Materials, National Science and Technology Council, Taipei 10622, Taiwan*

† Electronic supplementary information (ESI) available. See DOI: **https://doi.org/10.1039/d4tc02743d**

material, allowing the polar and magnetic instabilities to be separated onto different cations (as seen in the high-T_C perovskites $BiFeO_3$ and $BiMnO_3$[3,4]). However, this particular approach is inherently limited by the separate mechanisms producing ferroelectricity and magnetism, rendering device applications impractical due to the resultingly weak coupling between these effects.[5] If practical device applications based on multiferroic materials are to be realized, alternative approaches to multiferroism must be developed in which the coupling between the magnetic and electrical orderings is intrinsic by design.

A promising alternative route to magnetoelectric coupling is to exploit a combination of non-polar structural distortions and antiferromagnetic (AFM) orderings which, when combined, induce a polar distortion and weak ferromagnetism due to additional symmetry-breaking associated with their joint action.[6,7] Provided a material could be designed which combines these ingredients, and that some coupling between the primary magnetic and the non-polar order parameters exists, the required electric control of magnetization could be achieved. Such magnetoelectric coupling has already been predicted to occur, for example, in Ruddlesden–Popper perovskite-like materials.[8] More recently, this idea was extended to perovskite materials after enumerating the possible ways in which structural and magnetic symmetry-breakings can couple in the high-symmetry $Pm\bar{3}m$ aristotype structure.[9] These couplings can be used to determine the terms in a Landau-like energy expansion about the high-symmetry structure[10] up to arbitrarily high orders. Further details of our proposed scheme are given in the ESI,† as well as ref. 9, but we provide a brief summary here for context. Of particular importance to our scheme are terms in which the polarization (P) and magnetization (M) – transforming with respect to the $Pm\bar{3}m$ aristotype structure as the Γ_4^- and $m\Gamma_4^+$ irreducible representations (irreps), respectively – appear coupled linearly to other order parameters at the third order, as such terms can always adopt a sign so as to lower the free energy of the system. Provided the proposed combination of irreps which represent these order parameters (ξ) preserves crystal momentum, parity with respect to inversion symmetry, and time-reversal symmetry, this yields invariant terms in the Landau-like expansion of the form:

$$\mathrm{P}\xi_1\xi_2 \tag{1}$$

$$\mathrm{M}\xi_1\xi_3. \tag{2}$$

When present, a reversal of polarization in the invariant term (1) with an electric field must necessarily reverse either ξ_1 or ξ_2. If a material can be engineered in which it is energetically favorable to switch ξ_1 over ξ_2 in invariant (1) and M over ξ_3 in invariant (2), then a 180 degree reversal of magnetization with electric field – the exact mechanism desired for multiferroic memories – can be achieved. We illustrate a plausible scheme for this approach in Fig. 1.

In what follows, we explicitly demonstrate how our symmetry-informed magnetoelectric coupling scheme can be used to predict new multiferroic perovskites featuring intrinsic mechanisms of magnetoelectric coupling. We identify the new perovskite system $CeBaMn_2O_6$ as a promising prototype for our coupling scheme and confirm through first-principles simulations that the required symmetry-breaking ingredients represent the ground state of this system. We then present our experimental efforts to synthesize and characterize $CeBaMn_2O_6$ for the first time with the aid of high-pressure synthesis conditions, exploiting a combination of electron and neutron diffraction as well as magnetometry measurements to identify key signatures of the desired coupling scheme across a nanoscopic length scale. Our study showcases a promising new perovskite system in which to realize useful magnetoelectric coupling, as well as highlighting new opportunities to achieve magnetoelectric multiferroism within the perovskite structure type through the use of our innovative symmetry-adapted approach.

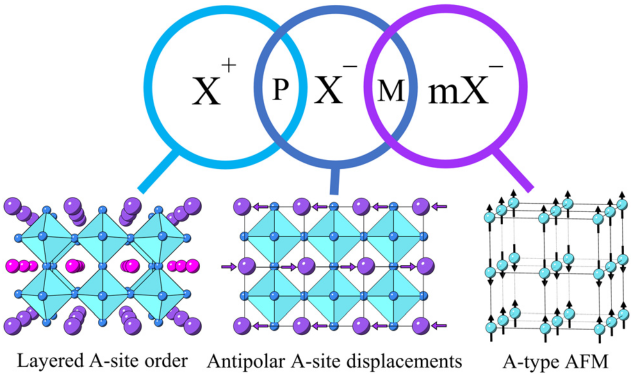

Fig. 1 An example scheme for inducing magnetoelectric coupling in the ABX_3 perovskite structure derived from the group-theoretical analysis in ref. 9. P and M denote irreps which describe ferroelectric polarization and weak ferromagnetism (wFM), respectively. These form two interdependent trilinear coupling terms defined as $Q(X^+)$ P $Q(X^-)$ and $Q(X^-)$ M $Q(mX^-)$ where the magnitude of a mode transforming as an X-point irrep, $Q(X)$, represents the actions of the ξ order parameters in (1) and (2). Examples of symmetry-breaking distortions which transform as these X-point irreps are also provided for reference. The X-point irreps have been labelled assuming the A site lies at the unit cell origin. Purple, magenta, and blue spheres represent the A(1), A(2), and X atoms, respectively, while cyan polyhedra represent the BX_6 octahedra; purple arrows denote displacement directions of the A cations, while black arrows denote spin moments on the B sites.

Materials and methods

Density functional theory calculations

To gain an understanding of structural, electronic and magnetic properties of $CeBaMn_2O_6$, we performed density functional theory (DFT) calculations as implemented in Vienna *ab initio* simulation package (VASP) Version 6.2.1.[11–13] Electronic structure calculations were performed using projected augmented wave (PAW) pseudopotentials in which the following electrons are treated as valence: Ce – $5s^25p^64f^15d^16s^2$, Ba – $5s^25p^66s^2$, Mn – $3p^63d^54s^2$, O – $2s^22p^4$. All other electrons are frozen to the atomic cores. The generalized gradient approximation (GGA) to the exchange–correlation functional is employed using the Perdew–Burke–Enzerhof parameterization for solids (PBESol)[14] with the additional Hubbard and Hund corrections of Liechtenstein *et al.* to better deal with the strongly correlated d and f electrons.[15] Previous computational studies[16,17] have found that U = 5 eV and J_H = 1.5 eV are appropriate for Mn^{3+} ions in $LaMnO_3$ and these are consequently the values we employ. We also utilize a high value of U = 10 eV and J_H = 0 eV on the strongly localized Ce f-states (see ESI,† for how the variations in U and J affect magnetic ordering). Energies and Hellman–Feynman forces were converged to less than 0.1 meV and 0.5 meV $Å^{-1}$ respectively, requiring a 1000 eV plane wave cutoff and a 4 × 4 × 3 Monkhorst–Pack *k*-point mesh.

Structural relaxations were performed using the conjugate gradient algorithm and continued until the largest force on any ion in the system was less than 1 meV $Å^{-1}$.

Non-collinear magnetic calculations with spin–orbit coupling[18,19] were utilized at two points. To calculate magnetocrystalline anisotropy energies, we performed non-self-consistent non-collinear magnetization calculations in which the self-consistent charge density from the collinear calculation was fixed and the energy calculated as the easy axis was varied. Fully self-consistent non-collinear calculations were also performed which required the increasing of the plane wave cut-off and Monkhorst–Pack grid to 1200 eV and 7 × 7 × 5 respectively to ensure convergence.

All symmetry analysis was conducted using the ISOTROPY Software Suite.[20,21] For the sake of brevity, we refer here to the order parameters and the associated order parameter directions (OPDs) simply by their irrep labels. Further details of the specific OPDs required to generate the magnetoelectric ground state consistent with our symmetry-adapted approach are provided in Note 1 (ESI†).

Synthesis

Polycrystalline samples with nominal composition $CeBaMn_2O_6$ were prepared by solid-state reaction under high-pressure and high-temperature conditions. First, a $BaMnO_3$ precursor was prepared at ambient pressure by mixing stoichiometric quantities of $BaCO_3$ (Alfa Aesar, 99.95%) and MnO_2 (Alfa Aesar, 99.997%) and heating to 1050 °C for 24 h. The single-phase $BaMnO_3$ precursor was then mixed with stoichiometric amounts of CeO_2 (Alfa Aesar, 99.99%) and MnO (Alfa Aesar, 99.99%) before being sealed in a platinum capsule. The capsule, boron nitride insulating layer and graphite heater were assembled in a pyrophyllite cube and placed in a DIA-type cubic anvil high-pressure apparatus. The samples were treated at 6 GPa and 1250 °C for 30 min before being rapidly quenched to room temperature and gradually released to ambient pressure. Each synthesis produced ~0.1 g sample. Laboratory X-ray powder diffraction patterns confirmed typical samples contained only minor impurity phases (witherite: ~2%, cerianite: ~0.5%, $Ba_4Mn_3O_{10}$: ~0.5%), demonstrating the nominal composition of our samples to be accurate.

Structural characterization

Synchrotron X-ray diffraction (XRD) data were collected on the I11 beamline at diamond light source, UK using a 15 keV energy beam and a position-sensitive MYTHEN detector. Refinement of a Si standard gave the precise X-ray wavelength as 0.82396(1) Å. A polycrystalline sample of $CeBaMn_2O_6$ was packed into a 0.1 mm capillary for the synchrotron measurements to minimize absorption effects. Neutron powder diffraction (NPD) data were collected on a combined 1 g sample at WISH, ISIS, UK (RB2010395-1).[22,23] Scans were recorded on cooling in the temperature range 1.5–300 K. Data were collected for 3 h at 1.5 K, 60 K, and 300 K, while for all other temperatures data were collected for 1 h. Rietveld refinements were performed with Topas using the jEdit interface.[24] Full crystallographic data obtained from the refinements are included in the ESI.†

Transmission electron microscopy (TEM) experiments were performed by mixing $CeBaMn_2O_6$ powder with fine (<10 μm) aluminum powder in a 1 : 10 ratio before being pressed using cold rollers to form a sheet ~100 μm in thickness. This sheet was mechanically thinned to ~20 μm and mounted on a copper support ring using epoxy resin before ion milling to electron transparency using Ar^+ ions at 6 keV. The specimen was finished using an ion beam energy of 100 eV to reduce surface damage to provide sufficiently thin edges for TEM. Samples were examined using a JEOL 2100 LaB_6 microscope operating at 200 kV.

Magnetic and physical characterization

DC magnetic susceptibility measurements were performed using a Quantum Design magnetic properties measurement system (MPMS). Zero-field-cooled (ZFC) and field-cooled (FC) magnetic susceptibility data were collected between 4 K and 300 K using a 500 Oe field. Magnetic hysteresis loops were recorded between 5 and 150 K in the range −5 to 5 T. DC resistivity data were collected on a polycrystalline bar of $CeBaMn_2O_6$ in the range 4–300 K with a Quantum Design physical property measurement system (PPMS) using a standard four-probe method. Our magnetic and physical property measurements evidence that the nominal oxidation states of Ce and Mn in our samples are +4 and +3, respectively, which is consistent with the oxidation states predicted by our DFT calculations. Further details of this analysis are provided in the ESI† (Note 2).

Results

Symmetry analysis and DFT calculations

In A-site layered perovskites, a trilinear coupling similar to (1) is known to induce ferroelectricity (Fig. 2a) *via* the hybrid improper ferroelectricity mechanism where the polarization is coupled to the A-site cation layering[25] (transforming as an X_1^+ irrep) and an antipolar motion of the cations (transforming as an X_5^- irrep). This establishes the polarisation coupling but, to conserve time-reversal symmetry and crystal momentum, restricts ξ_3 in eqn (2) to be a distortion representing an A-type magnetic structure (transforming as an mX_5^- irrep). One such perovskite material with this spin ordering is $LaMnO_3$,[26] which we describe here using the *Pnma* setting. The magnetic

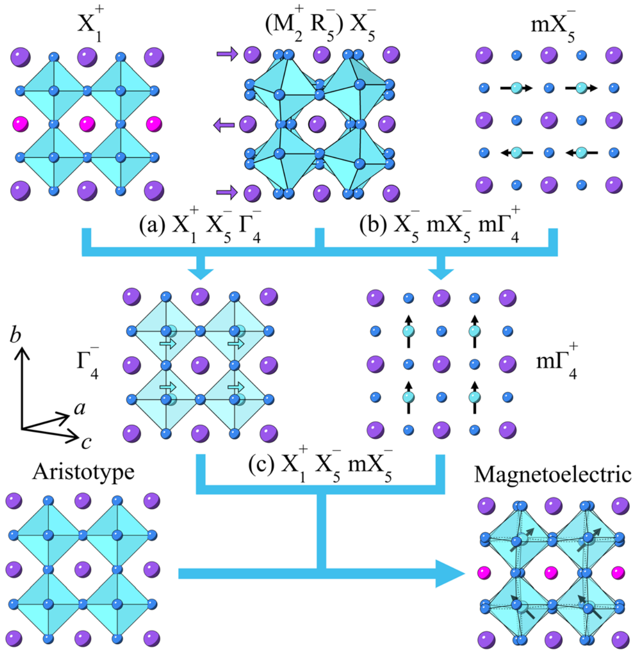

Fig. 2 The desired crystallochemical features required to achieve a magnetoelectric ground state in an A-site layered perovskite such as $CeBaMn_2O_6$. The combination of layered A-site order (X_1^+), antipolar A-site displacements (X_5^-), and A-type AFM order (mX_5^-) feature in the two trilinear coupling terms (a) and (b), yielding a ferroelectric polarization (Γ_4^-) and a ferromagnetic component ($m\Gamma_4^+$), respectively. Both (a) and (b) trilinear coupling terms are mutually coupled *via* the action of the X_5^- term, which itself emerges through a separate trilinear coupling term with the M_2^+ and R_5^- octahedral tilt modes as detailed in ref. 28. The trilinear terms (a) and (b) ultimately conspire to yield the desired magnetoelectric switching, taking the form of the term (c). Full details of the desired order parameter directions for these coupling terms can be found in the ESI.† Representative axes labels are shown with respect to the *Pnma* structure, upon which we base our subsequent discussion.

moments in the *ac* plane align ferromagnetically and interactions between planes are AFM. This magnetic structure also allows for a weak ferromagnetic canting[27] (Fig. 2b) so that upon a reversal of the ξ_1 (X_5^-) ordering in eqn (2), it is much more likely for the wFM produced magnetization M to reverse than the dominant A-type AFM order (Fig. 2c). In reality, any reversal of the X_5^- mode would most likely occur through a concomitant switching of the *Pnma*-type octahedral tilt configuration (described as transforming as the M_2^+ and R_5^- irreps) as there exists a separate trilinear coupling term of the form $M_2^+ R_5^- X_5^-$.[28] Thus, any magnetoelectric switching in this material would most likely involve the octahedral tilting configuration so as to effectively control the intermediary antipolar A cation displacements and enable the desired electric–field control over M.

Evidently, both the polarization and its coupling to the reversal of magnetization can be achieved by inducing an A-site cation layering to $LaMnO_3$ without changing the magnetic structure. As the magnetic structure is determined *via* the superexchange paths,[29–31] which are themselves dependent on the degree of octahedral tilting and the C-type orbital order present in this perovskite, it is assumed that ordering the A sites with cations that do not change the valence state or drastically alter the tolerance factor will leave the magnetic structure unaffected. For this reason, we choose an isoelectronic substitution of La layers with alternating layers of Ce^{4+}/Ba^{2+} as the average ionic radii of these two cations is similar to La^{3+} ($\langle r_A \rangle$ (XII) = 1.375 Å *vs.* $r_{La^{3+}}$ (XII) = 1.36 Å). Although not changing the tolerance factor, we anticipate that the largely differing charges and radii of Ce^{4+} (r = 1.14 Å) and Ba^{2+} (r = 1.61 Å) should favor the formation of a cation ordered phase, with A-site layering being the most commonly observed ordering configuration for double perovskites.[25]

In $LaMnO_3$, the combined effect of the Jahn–Teller active Mn^{3+} and low Goldschmidt tolerance factor result in a cooperative Jahn–Teller distortion (accompanied by a C-type orbital ordering of the $|x^2\rangle$ and $|z^2\rangle e_g$ orbitals) and an $a^-b^+a^-$ octahedral tilt pattern. The Jahn–Teller distortion acts as the gapping mechanism and the overlapping e_g orbitals supply the A-type AFM *via* the Goodenough–Kanamori–Anderson rules. Given the similar average ionic radii of Ce^{4+}/Ba^{2+} to La^{3+}, we expect the same conclusions to hold for the layered $CeBaMn_2O_6$ structure.

To test these ideas, we performed a full structural relaxation for each of the four magnetically ordered structures available in the $CeBaMn_2O_6$ *Pnma* crystal structure (A-type AFM, C-type AFM, G-type AFM and FM). This revealed that A-type AFM is lowest in energy with FM ordering 13.02 meV per f.u. higher while G-type and C-type AFM are 44.3 meV per f.u. and 54.5 meV per f.u. higher than the ground state AFM, respectively. It should be noted that varying the Hubbard-*U* parameterization results in a transition to a ferromagnetic ground state (Fig. S3, ESI†). The A-type AFM required for our proposed coupling scheme is stable within the range $3\text{ eV} < U < 6\text{ eV}$ – a result consistent with analogous studies on $LaMnO_3$. Altering the Hubbard-*U* on the Ce^{4+} ion does not change the magnetic structure away from A-type AFM. Furthermore, we calculated the magnetic moment on each Mn ion to be $3.707\mu_B$ – this value suggests the Ce^{4+} oxidation state rather than Ce^{3+}. This oxidation state is further supported by the calculated electronic band structure (Fig. S3, ESI†) displaying empty Ce f bands and also by electronic structure calculations on a ferromagnetic structure in which the total magnetization is $4\mu_B$ per f.u. suggesting a Mn^{3+} state (and consequently a Ce^{4+} state). Subsequent DC resistivity measurements on the synthesized samples substantiated these oxidation state assignments (Note 2, ESI†).

With A-type AFM identified as the ground state, we calculated the electronic band gap (Fig. S3, ESI†) of this system to be 0.98 eV – lower than the 1.7 eV measured in $LaMnO_3$.[32] One should keep in mind the difficulty in calculating accurate band gaps within DFT[33] and the strong dependence of bandgap on the choice of Hubbard-*U* correction. Table S1 (ESI†) contains a detailed comparison of how the simulated structures of $LaMnO_3$ and $CeBaMn_2O_6$ differ. We note that the calculated amplitude of the R_5^- tilt mode is slightly smaller in $CeBaMn_2O_6$ compared to $LaMnO_3$, which may also contribute to the lower band gap we obtain for this system.

These two conditions – A-type AFM and the occurrence of a bandgap – are all that are strictly necessary for determining the feasibility of our coupling scheme in $CeBaMn_2O_6$ assuming A-site cation layering and a *Pnma* tilt scheme. The appearance of a polar distortion and weak ferromagnetism determined by antisymmetric exchange interactions are guaranteed by the crystal symmetry. Using the Berry phase formulation of the modern theory of polarization,[34] we calculate an electric polarization of 9.90 $\mu C\ cm^{-2}$ parallel to the crystallographic *a* lattice vector which is similar to the magnitude of polarization calculated for other improper-ferroelectric multiferroics such as $YMnO_3$ ($P \approx 6.5\ \mu C\ cm^{-2}$).[35] This polarization direction is predicted due to the antipolar displacements of the A cations along the *a* axis, which are uncompensated due to the cation layering hence they enable polarization to emerge along the same axis.

$LaMnO_3$ is reported as having a weakly ferromagnetic component to its spin structure as is allowed by symmetry. When we included the effects of relativistic spin–orbit coupling in our DFT simulation, we were able to calculate the magnetocrystalline anisotropy energies and determine the easy axis with associated spin canting directions for $CeBaMn_2O_6$. We determined (Table S2, ESI†) that the energetically favorable easy axis was the [100] direction in the orthorhombic cell, a result that is also found in $LaMnO_3$.[27] This easy axis allows a spin canting which produces a ferromagnetic component of $0.029\mu_B$ per Mn along the long *b* axis.

Finally, we note that the reversal of X_5^- requires either the reversal of the in-phase tilts (M_2^+) or the antiphase tilts (R_5^-) – see the top panel of Fig. 2. Whichever of these intermediate modes are reversed, the subsequent electric-field reversal of the wFM is required by symmetry (Fig. 2b). Taken together, these factors demonstrate that $CeBaMn_2O_6$ contains all the necessary ingredients and coupling to make it a promising magnetoelectric multiferroic. Equipped with this theoretical insight, we attempted to synthesize $CeBaMn_2O_6$ as a prototype for our magnetoelectric coupling scheme.

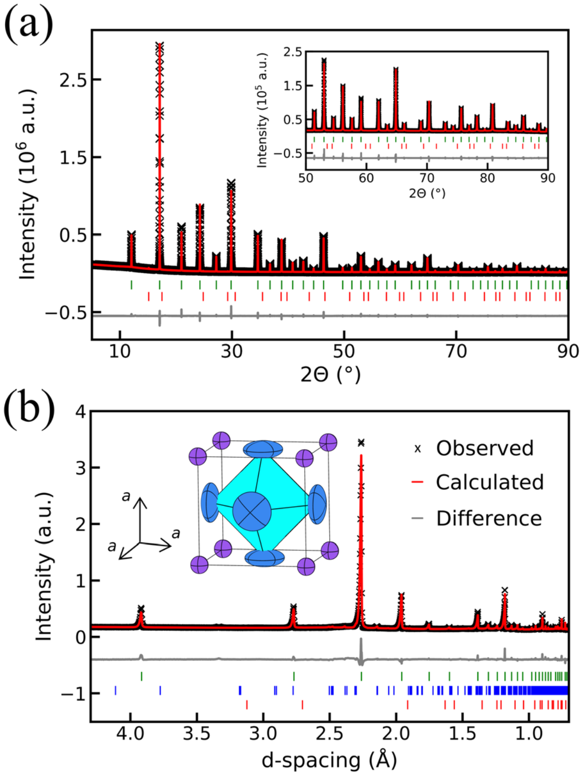

Fig. 3 Rietveld fits using a $Pm\bar{3}m$ structural model against (a) synchrotron XRD data collected on the I11 beamline at Diamond Light Source, UK (λ = 0.82396 Å), and (b) NPD data collected on the backscattering bank at WISH at 300 K. The fit against the data collected on the backscattering bank is depicted in (b), though data from all banks were used to refine the structural model. Green, blue, and red tick marks correspond to Bragg reflections for $CeBaMn_2O_6$, $Ba_4CeMn_3O_{12}$ (~3 wt%), and CeO_2 (~0.4 wt%), respectively; note that different impurities are observed in the WISH experiment due to the use of a combined ~1 g sample. The inset in (b) depicts the refined $Pm\bar{3}m$ structural model for $CeBaMn_2O_6$ at 1.5 K, highlighting the large anisotropic displacement parameters for the oxygen sites at this temperature (drawn at 95% probability).

Synthesis and crystal structure

Previous attempts to synthesize $CeBaMn_2O_6$ at ambient pressure were reportedly unsuccessful as no perovskite-type compound could be stabilized.[36] We found that our own samples prepared at ambient pressure typically contained large amounts of CeO_2 impurity (>10 wt%) so that the desired composition could not be prepared this way. High-pressure synthesis methods have been shown to promote cation ordering in perovskite materials,[37–39] so we pursued this strategy to prepare phase-pure samples of $CeBaMn_2O_6$. Synchrotron XRD data collected at room temperature revealed our samples synthesized at 6 GPa could be indexed to a perovskite-type phase. Only minor impurity phases such as CeO_2 (~0.4 wt%) could be observed in our best samples, showing the desired composition can be suitably prepared in this manner. Surprisingly, our Rietveld fits against synchrotron XRD data (Fig. 3a) find that the data are modelled well by cubic $Pm\bar{3}m$ symmetry at room temperature, and we detected no additional Bragg reflections or peak splitting to suggest any lowering of symmetry from the aristotype structure. This was corroborated by performing Rietveld fits to NPD data measured in the range 1.5–300 K (Fig. 3b), which confirmed that the average crystal structure is well described by $Pm\bar{3}m$ symmetry across this temperature range. Any attempts to fit lower-symmetry models accounting for long-range cation ordering or octahedral tilting did not improve the quality of the Rietveld fits. Full crystallographic details obtained from the Rietveld refinements can be found in the ESI† (Tables S3–S5).

Other $LnBaMn_2O_6$ (Ln = lanthanide) perovskite systems are highly sensitive to the presence of cation disorder on the A site, wherein the heterogeneous distribution of Ln^{3+} and Ba^{2+} cations suppresses long-range octahedral tilting and favors disordered or glassy electronic ground states.[40–42] Extreme cation disorder would make any superstructure reflections far too broad or diffuse to observe by XRD/NPD, explaining why the $Pm\bar{3}m$ aristotype model most appropriately describes the average symmetry of $CeBaMn_2O_6$. However, the diffraction peaks in the synchrotron XRD/NPD patterns remain sharp, suggesting there is no phase separation of Ce- or Ba-rich domains.

Based on our Rietveld fits against high-resolution synchrotron XRD data, we estimate our samples exhibit very little microstrain (e_0 = 0.015%). This implies that any deviation from the macroscopic average cubic lattice parameter in our samples must be exceptionally small, effectively discounting the existence of any severe chemical inhomogeneity. Taken together, the observation of a macroscopic cubic lattice and very low microstrain imply spatial homogeneity of Ce/Ba, but any periodic A-site ordering must be shorter than the length scales over which strains relax in typical perovskites oxides (*e.g.* over ∼50 unit cells, ∼20 nm). We have arrived at this upper estimate for the length scale over which macrostrain will not relax in our system by considering the observed rates of relaxation of epitaxial strain in $LaAlO_3/SrTiO_3$ interfaces,[43] which finds that for less than 50 unit cells (∼20 nm) the $LaAlO_3$ relaxes less than the microstrain value of 0.015% in $CeBaMn_2O_6$. Our relaxed DFT model for A-site ordered $CeBaMn_2O_6$ has macrostrain values of ∼6%, whereas the epitaxial strain between $LaAlO_3/SrTiO_3$ is only 2.7% in ref. 43, so we view this 20 nm distance as the absolute maximum length scale over which any cation ordering can occur given that average cubic symmetry is still observed in our X-ray diffraction experiments.

Our refinements against NPD data showed that the displacement parameters for the oxygen sites are highly anisotropic (U_{11} = 0.018(1) Å^2, $U_{22} = U_{33}$ = 0.078(1) Å^2) even at 1.5 K, reflecting significant static disorder of the oxygen positions. The large U_{33} corresponds to a root-mean-square (rms) displacement of 0.28 Å, which is about half the difference between the Ba^{2+} and Ce^{4+} radii, implying that the oxygen atoms on average sit halfway between the optimum positions for Ba and Ce but are locally relaxed. The oblate shape of the displacement ellipsoids at 1.5 K (drawn in Fig. 3b at 95% probability) suggests the MnO_6 octahedra are statically tilted, albeit only across short length scales that are inaccessible to our synchrotron XRD and NPD experiments.

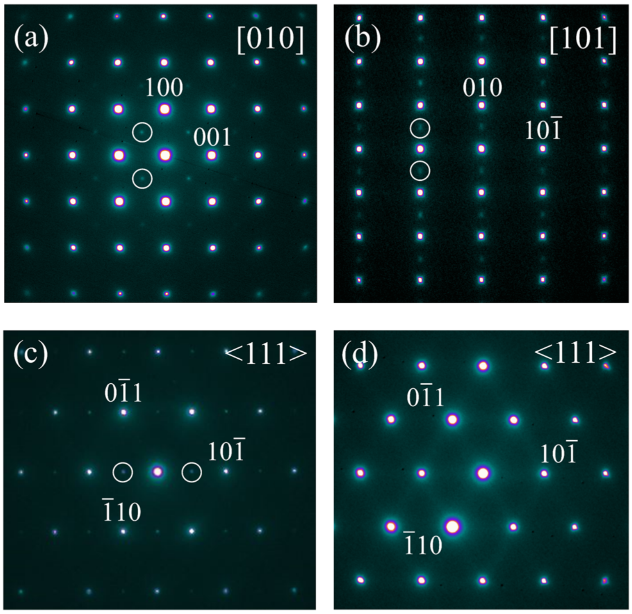

Fig. 4 SAED patterns of $CeBaMn_2O_6$ indexed with zone axes (a) [010], (b) [101], and (c) [111]. Superstructure reflections (circled) can be indexed with propagation vectors of $\boldsymbol{k}$ = (1/2, 0, 1/2) in both (a) and (c), and $\boldsymbol{k}$ = (0, 1/2, 0) in (b). The ⟨111⟩ zone-axis diffraction pattern in (d) is provided as an example of a crystallite featuring streaks of diffuse scattering along the $\langle 10\bar{1}\rangle$ directions, rather than discrete superstructure reflections.

To investigate the possibility of short-range octahedral tilting in $CeBaMn_2O_6$, we collected selected-area electron diffraction (SAED) patterns on several crystallites (Fig. 4). Electron diffraction is advantageous over X-ray or neutron diffraction in this respect as diffraction data can be collected across much smaller regions, effectively enabling the structural details of individual domains to be probed. Combined with the stronger scattering interactions of electrons, SAED should be significantly more sensitive to any octahedral tilting distortions with short coherence lengths. Fig. 4 shows that various sets of weak superstructure reflections can be distinguished across several zone axes, each imaged from different crystallites: the reflections in Fig. 4a and c can be indexed with the propagation vector $\boldsymbol{k}$ = (1/2, 0, 1/2), consistent with reflections at the M point, while the reflections in Fig. 4b can be indexed with the propagation vector $\boldsymbol{k}$ = (0, 1/2, 0), consistent with reflections at the X point. The combined set of superstructure reflections reveals the adoption of a $\sqrt{2}a_p \times 2a_p \times \sqrt{2}a_p$ (where a_p is the primitive cubic lattice parameter) superstructure of the parent $Pm\bar{3}m$ cell on a nanoscopic length scale. These superstructure reflections map exactly onto those observed for *Pnma* (*Pbnm* in non-standing setting) perovskites such as $CaTiO_3$,[44] demonstrating that $CeBaMn_2O_6$ adopts the same $a^-b^+a^-$ ($a^-a^-c^+$) tilt pattern. The M-point superstructure reflections in Fig. 4c hence correspond to in-phase octahedral rotations about the *b* axis, which, in the language of our group-theoretical approach, transform with respect to the $Pm\bar{3}m$ aristotype (with A site at the origin) as the M_2^+ irrep. The X-point superstructure reflections can be attributed to so-called concert reflections[45,46] which arise in perovskites featuring both in-phase and antiphase octahedral tilting simultaneously.[44] Physically, these reflections correspond to antipolar motions of the A cations which transform with respect to the $Pm\bar{3}m$ aristotype as the X_5^- irrep. In *Pnma*-type perovskites, antipolar motions of the A cations are guaranteed to occur by symmetry due to a trilinear coupling term of the form $M_2^+ R_5^- X_5^-$, so our observation of the M_2^+ and X_5^- modes allows us to infer the presence of the antiphase octahedral tilt mode R_5^- as well. Although we have only been able to sample diffraction patterns from three possible zone axes to make this assignment, we note these three alone are sufficient to distinguish $a^-b^+a^-$ from all other possible mixed-tilt systems (Table S6, ESI†), granting a high degree of confidence in the assignment of the $a^-b^+a^-$ tilt scheme in $CeBaMn_2O_6$. We note that layered cation ordering should also transform as an X-point irrep, so we cannot interrogate the cation arrangement directly from our SAED patterns. Indeed, the SAED reflection conditions predicted for a cation-disordered *Pnma* perovskite are identical to that expected for a *Pnma*-type perovskite featuring cation layering along the long *b* axis,[44,47] so we primarily use our current SAED data to evidence the *Pnma*-type octahedral tilt configuration.

While most of the crystallites we selected exhibited discrete superstructure reflections, we noted that some exhibit streaks of diffuse scattering instead (Fig. 4d). Such diffuse scattering suggests that the coherence length of the $a^-b^+a^-$ tilting is limited within these regions. To probe the coherence length of the tilting within our sample, we performed dark field imaging based on the (0, $\frac{1}{2}$, 0) superstructure reflection (Fig. 5). This revealed a highly mottled contrast across a ~200 nm length scale (Fig. 5b), reflecting an intricate mixture of tilted and untilted nanoscale domains. A line analysis of the image contrast (Fig. 5c) showed that the domains are typically 5–10 nm in size, with an average size of 7 ± 2 nm. This corresponds to approximately 20 unit cells with respect to the primitive cubic lattice parameter (~3.9 Å), which is well below the length scale typically required to resolve Bragg reflections in X-ray or neutron diffraction. This estimate also agrees well with the maximum coherence length of cation ordering we derived based on the extent of microstrain in our samples.

Our electron diffraction and microscopy experiments indicate that the *Pnma* tilt scheme – hence the antipolar displacement of the A cations – is obtained in $CeBaMn_2O_6$, but that the coherence length of these distortions appears to be limited by the presence of cation disorder between the Ce and Ba atoms. With this knowledge, we re-examined the possibility of any short-range *Pnma*-like reflections in our XRD/NPD patterns. We generated a $\sqrt{2}a_p \times 2a_p \times \sqrt{2}a_p$ *Pnma* superstructure of the parent $Pm\bar{3}m$ cell using ISODISTORT[21] and performed a symmetry-mode refinement of this model against our 1.5 K NPD data collected on the backscattering bank at WISH. We applied an *hkl*-dependent Lorentzian convolution to the *Pnma*-type reflections to account for possible size-dependent (Scherrer) superstructure peak broadening due to short-range M_2^+ and R_5^- tilt modes with a full-width half-maximum (FWHM) that varies as:

$$\mathrm{FWHM} = 0.1\mathrm{DIFC}d^2/S \tag{3}$$

where DIFC, d, and S correspond to the diffractometer constant, d-spacing, and the domain size, respectively. Fig. S4 (ESI†) shows that this *Pnma*-like model accounts for regions of diffuse scattering observed in the diffraction patterns. The refined model is shown in Fig. S5 (ESI†), and selected parameters obtained from the refinements are provided in Table S8 (ESI†). We found no notable temperature dependence for any of these parameters, indicating that the short-range order is largely static rather than dynamic in origin. R_{wp} decreases from 6.35% ($Pm\bar{3}m$, refined parameters = 16) to 5.24% (constrained *Pnma*, refined parameters = 18), reflecting a clear improvement in the quality of fit with this approach. The amplitudes of the M_2^+ and R_5^- tilt modes refine to be 0.36(2) Å and 0.58(1) Å, respectively. These are smaller than predicted by our relaxed DFT structure (Table S2, ESI†) due to strong correlations with the background terms in our refinements as well as the disordered nature of the tilting. The equivalent isotropic displacement parameters on the oxygen sites decrease significantly with the use of the *Pnma*-type model ($U_{\mathrm{iso}}(Pnma)$ = 0.006(1) $Å^2$ *vs.* $U_{\mathrm{iso}}(Pm\bar{3}m)$ = 0.029(1) $Å^2$), demonstrating how the $a^-b^+a^-$ tilt pattern successfully describes the static positional disorder associated with the oxygen site in the $Pm\bar{3}m$ model. Including the size of the *Pnma*-like domains as a fitting parameter yields an average domain size of 4.3(3) nm. We note that this parameter will also be strongly correlated to the background terms, preventing an accurate estimate of the average domain size. Nevertheless, this estimate agrees well with the domain size obtained from our dark-field image analysis.

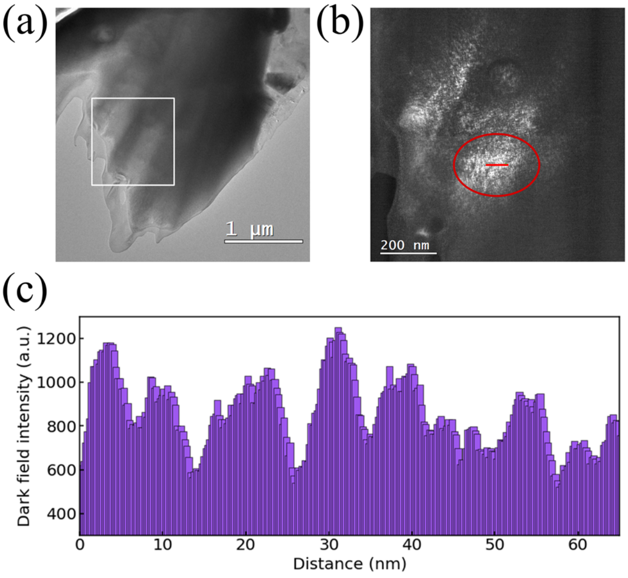

Fig. 5 (a) TEM image of the $CeBaMn_2O_6$ crystallite used to perform dark-field imaging. The white box indicates the region over which the dark-field image was collected. (b) Dark-field image using the (0, $\frac{1}{2}$, 0) superstructure reflections observed by SAED, with white and black corresponding to regions where the reflection is observed and absent, respectively. The region circled in red corresponds to the area chosen to analyze the domain sizes. (c) Line profile of the domain sizes based on the red line shown in (b).

Magnetic characterization

Our NPD data revealed that no magnetic Bragg reflections emerge upon cooling to 1.5 K, showing there is no long-range magnetic order of the Mn moments. As previously stated, cation disorder is known to suppress long-range magnetic order in favor of glassy spin textures.[48–50] This is most likely why no long-range magnetic order is observed in $CeBaMn_2O_6$. Nevertheless, close inspection of the NPD data reveals the emergence of a broad diffuse scattering contribution at high d-spacing (~8 Å) upon cooling (Fig. 6a), which is consistent with the presence of some short-range magnetic order. By modelling the diffuse scattering peak with a simple pseudo-Voigt function, we determined that the diffuse scattering component emerges below 100 K and becomes more intense upon further cooling (Fig. 6b). Based on the data collected at 1.5 K, where the diffuse scattering contribution is most prominent, we extract a more precise peak position of d = 7.9(1) Å. This is within 1σ of double the refined cubic lattice parameter at this temperature (a = 3.90966(7) Å), demonstrating that the short-range

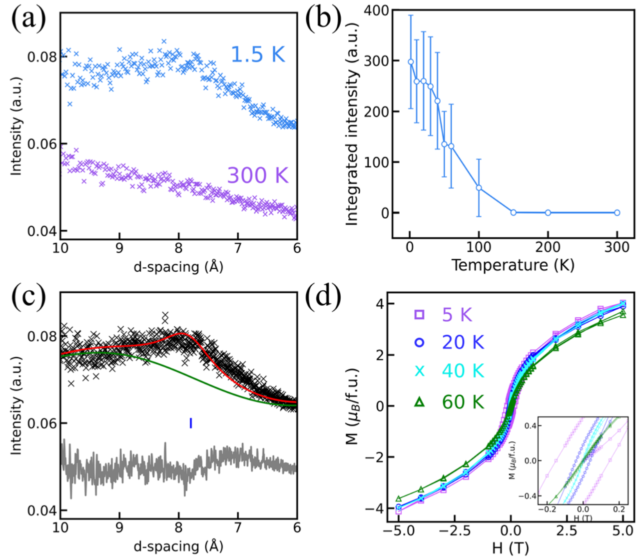

Fig. 6 (a) The emergence of diffuse magnetic scattering in $CeBaMn_2O_6$, as observed in NPD data collected on WISH on the 58° bank. The diffraction patterns at 1.5 K and 300 K have been offset from one another for visual clarity. (b) Temperature-dependent integrated intensities of the diffuse scattering peak centered at $d \approx 8.0$ Å, as determined by fits to a pseudo-Voigt function. (c) Rietveld fit against the magnetic diffuse scattering region using the magnetic mX_5^- mode. The background line (green) has been depicted to highlight the additional scattering contribution from the mX_5^- mode. (d) Isothermal magnetization (*M*) *vs.* applied field (*H*) loops of $CeBaMn_2O_6$ measured at 5 K (purple squares), 20 K (blue circles), 40 K (cyan crosses), and 60 K (green triangles). The inset highlights the hysteresis observed below 40 K.

magnetic ordering arrangement responsible for the diffuse scattering can be related to the $Pm\bar{3}m$ aristotype using the propagation vector $\boldsymbol{k} = (1/2, 0, 0)$. Our DFT calculations predict that the magnetic ground state should be A-type AFM, consistent with the experimentally observed $\boldsymbol{k}$ vector. In this structure, the Mn^{3+} moments are aligned antiferromagnetically along the *Pnma* *b* axis and ferromagnetically within the *ac* plane (as shown in Fig. 2). This magnetic structure transforms with respect to the $Pm\bar{3}m$ aristotype as the mX_5^- irrep, in which the moments must lie in the plane perpendicular to *b* if magnetic Bragg intensity is to be observed for the $(010)_{Pnma}$ reflection. Fig. 6c shows that the inclusion of an mX_5^- mode in the Rietveld fit (corresponding to magnetic space group $Pn'm'a$, no. 62.446), combined with a similar size-broadening term used to model the octahedral tilt modes, successfully captures the diffuse scattering contribution. From the initial Rietveld fit, we extract a magnetic moment of $\mu(\underline{x}) = 0.65(7)\mu_B$ per Mn; this value is likely underestimated compared to the true magnitude of the Mn moment due to the strong correlation with the background terms, as previously noted for the magnitude of the octahedral tilt modes. Upon performing a background subtraction between the low- and high-temperature datasets, the ordered moment was subsequently refined to be $2.8 \pm 1.3\mu_B$, which is within 1σ of the expected moment for Mn^{3+} ($S = 2$). The metrically cubic lattice parameters prevent us from assigning the specific orientation of the Mn^{3+} moments within the *ac* plane based on the present Rietveld analysis, so here we choose to orient the moments along *a* in accordance with the magnetic easy axis identified from our DFT calculations (Table S2, ESI†). From our Rietveld fit, we extract a magnetic domain size of 5.8(4) nm. This agrees well with the value estimated by our dark-field image analysis as well as that obtained from fitting our short-range *Pnma*-type model to our diffraction data, showing the structural and magnetic domains are similar in size as would be expected if their orderings were intrinsically linked. Simulated diffraction patterns confirm that the only alternative X-point magnetic ordering configuration (transforming as an mX_1^- irrep) should not produce any magnetic scattering at this *d*-spacing (Fig. S6, ESI†). This irrep corresponds to an A-type AFM order with the Mn^{3+} moments oriented along *b*, so we can exclude the possibility of this magnetic structure in $CeBaMn_2O_6$. We also exclude the possibility of alternative AFM orderings, such as C-type or G-type AFM, as these magnetic structures are described by different propagation vectors that do not transform as an X-point irrep.[9] Accordingly, we uniquely identify the mX_5^- mode as responsible for the diffuse scattering feature we observe in our diffraction experiments, in accordance with the magnetic structure predicted by our DFT calculations.

ZFC and FC DC magnetic susceptibility measurements (Fig. S7, ESI†) reveal $CeBaMn_2O_6$ is paramagnetic at room temperature. Fitting a Curie–Weiss expression above 150 K yields a Curie constant of $C = 5.96(1)$ emu K^{-1} mol^{-1}. This corresponds to an effective moment of $4.89\mu_B$, which is in excellent agreement with the spin-only value expected for Mn^{3+} ($\sim 4.90\mu_B$). Upon cooling, the ZFC and FC traces diverge below ∼38 K, but the lack of any long-range magnetic reflections in the NPD patterns confirms this is not due to a long-range ordering of the Mn moments. Our synchrotron XRD experiments found no evidence of trace magnetic impurities such as Mn_3O_4 which might otherwise explain this feature. Similar behavior has been observed in other cation-disordered $LnBaMn_2O_6$ (Ln = Y, Dy–Sm) materials,[41,51] where divergences between ZFC and FC traces arise due to the freezing of short-range AFM spins with a wFM component, so we attribute this as the origin of the ZFC-FC divergence in $CeBaMn_2O_6$. Isothermal magnetization measurements (Fig. 6d) show a clear ferromagnetic hysteresis develops below the spin freezing transition. Weak ferromagnetic spin canting is predicted by our design scheme due the coexistence of atomic displacements transforming as X_5^- and magnetic ordering transforming as mX_5^-, giving the desired trilinear term with $m\Gamma_4^+$ which describes the character of the wFM representation in $Pm\bar{3}m$ perovskites.

Discussion

Our experimental insight demonstrates that the individual ingredients required for magnetoelectric coupling are present in $CeBaMn_2O_6$, and these appear to coexist spatially within the same regions of the sample. However, the coherence length of the antipolar cation displacements and A-type AFM ordering is very short, most likely a consequence of the limited extent of cation ordering within our samples. Such cation disorder also disrupts symmetry-breaking in several other $LnBaMn_2O_6$ systems. For example, in $NdBaMn_2O_6$ the cation-ordered material adopts the $a^-b^+a^-$ tilt system below 340 K[52] whereas the disordered counterpart exhibits average $Pm\bar{3}m$ symmetry at these temperatures.[40] Previous electron diffraction studies on $SmBaMn_2O_6$ also found that cation disorder across the A site imposes a random potential effect, inhibiting the coherence length of charge and orbital orders on the Mn^{3+}/Mn^{4+} sites such that average $Pm\bar{3}m$ symmetry is observed.[51] However, in these examples, the disordered materials show no signs of any appreciable superstructure across either global or local length scales, suggesting the cation distributions in these cases were too randomized for any signatures of symmetry-breaking to emerge. Our observation of discrete superstructure reflections as well as diffuse scattering by SAED and NPD strongly suggests the cation distribution in our samples is not completely randomized such that the spatial correlations governing octahedral tilting and A-type AFM are mediated by some form of short-range chemical order. Such behavior is well established in other partially disordered perovskites, particularly lead-based relaxor ferroelectrics wherein the emergence of both long-range polarization and the relaxor-type behavior depend upon the short-range nature of chemical ordering across the B site.[53,54] The appearance of short-range cation displacements and A-type AFM in $CeBaMn_2O_6$ therefore implies there is also some degree of cation ordering present, at least across the nanoscopic length scale. To achieve bulk magnetoelectric coupling, it is important to consider why the cation ordering in this system is only short-range and how this may be controlled.

We returned to our DFT calculations and performed full geometry relaxations on a selection of alternative cation orderings. These are enumerated, along with their energies, in Table S8 (ESI†). Each structure is strained significantly from the aristotypical cubic structure (where $a_p \approx 3.9$ Å), so the lack of any discernable peak splitting in our diffraction patterns shows that none of these alternative cation configurations nor any of their associated symmetry-breakings achieve any long-range coherence in our samples. Interestingly, we find that the assumed Ce/Ba layering perpendicular to the [010] direction (space group: $Pmc2_1$) is not the ground state cation configuration from the perspective of DFT: instead, alternative X-point layerings along either [100] or [001] are the most energetically favorable configurations. Layering along the [001] direction results in a polar space group (Pm), while layering along [100] produces a non-polar space group ($P2_1/m$). The Pm structure contains the same collection of modes necessary for the switching scheme as for the $Pmc2_1$ structure illustrated in Fig. 2, so this is likely another prospective candidate phase for magnetoelectric switching within this system. Both [001] and [100] layering directions have energies within kT of the sample synthesis temperature ($\sim$0.1 eV per f.u.), so we anticipate small regions of the sample will nucleate with different configurations of cation ordering. Furthermore, although A-site ordering with layering perpendicular to [010] has higher ground state energy, it being the highest-symmetry phase means that at elevated temperatures it may become entropically favorable, hence all three layering configurations may become feasible under the synthesis conditions we have employed. Nevertheless, the competition from alternative cation ordering arrangements appears to be sufficient to disrupt any long-range cation ordering throughout the bulk of the material.

Further efforts to achieve magnetoelectric coupling in $CeBaMn_2O_6$ should focus on improving the coherence length of cation ordering beyond nanoscale domains. It is highly likely our use of high-pressure synthesis conditions has been crucial in promoting any partial cation ordering: $LnBaMn_2O_6$ (Ln = Y, lanthanide) materials synthesized at ambient pressure typically require a preliminary reduction step to achieve cation ordering,[25,41] so the use of even higher synthesis pressures may assist in increasing the size of the symmetry-lowered domains. Cation layering has also been proposed to be favored by large cation size variance in hydrothermally synthesized $La_{0.5}Tb_{0.5}CrO_3$ (σ^2 = 0.004 Å^2). Here, hydrothermal methods avoid the high temperatures typically required for solid-state reactions and thus prevent reorganization of the A cations into a disordered array.[55] Based on the nominal Ce^{4+} valence, we expect $CeBaMn_2O_6$ to have a much larger size variance of σ^2 = 0.051 Å^2 (this value is calculated based on the 9 co-ordinate ionic radii; we have taken a linear interpolation of the 8 and 10 co-ordinate radii of Ce^{4+} to calculate $r_{Ce^{4+}}$ (IX)). To the best of our knowledge, $CeBaMn_2O_6$ has the largest reported size variance of any A-site substituted perovskite, so hydrothermal synthesis may be a promising alternative synthesis route to achieve long-range cation ordering in this system and to experimentally verify the ground state cation ordering configuration. Finally, we anticipate that epitaxial growth techniques will be key to ensure control over the directionality of the cation ordering within this system, thus ensuring the cation configuration is compatible with the magnetoelectric coupling scheme we have outlined in this work and potentially enabling magnetoelectric coupling to be realized beyond the nanoscale achieved in our high-pressure-synthesized samples.

Summary

Our symmetry-informed approach has identified the new manganite perovskite $CeBaMn_2O_6$ as a promising system in which to achieve magnetoelectric multiferroism. High-pressure synthesis methods have been crucial to stabilize highly pure samples of this new perovskite composition for the first time, and our diffraction and physical property characterization measurements have revealed clear signatures of the critical symmetry-lowering ingredients required for multiferroicity within spatially coherent regions of the sample. Our findings are consistent with the theoretical predictions of our DFT calculations, highlighting the value of our symmetry-adapted approach in designing new magnetoelectric perovskites. Our DFT calculations have rationalized the limited coherence length of the multiferroic domains in our synthesized samples as being due to the competing cation ordering configurations which appear to nucleate due to having ground state energies within *kT* of the synthesis temperature. Controlling the directionality of the cation layering in this system will be key to enhance the size of these symmetry-lowered domains so that magnetoelectric coupling can be achieved across the bulk of the material for device applications. While we have explicitly applied our design scheme with respect to various X-point orderings within the perovskite structure type, we note the wealth of additional lattice, spin, charge, and orbital orderings possible in perovskite materials (which can arise at different ***k*** points) offers many further opportunities to realize additional magnetoelectric couplings beyond what we have outlined in this work. Finally, further exploration of the compositional space offered by perovskite materials, guided by our symmetry-informed design scheme, should allow for numerous new magnetoelectric candidates to be identified beyond the $CeBaMn_2O_6$ system we have studied in this work, paving new directions in the search for room-temperature magnetoelectric multiferroics.

Author contributions

S. S. and C. A. M. S. contributed equally to this work. The manuscript was written through contributions of all authors. All authors have given approval to the final version of the manuscript.

Data availability

Data supporting this article have been included as part of the ESI.†

Conflicts of interest

There are no conflicts of interest to declare.

Acknowledgements

M. S. S. acknowledges the Royal Society for a fellowship (grant no. UF160265 and URF\R\231012) and the EPSRC for funding (grant no. EP/S027106/1), through which S. S. was supported. The synchrotron powder diffraction data were collected on I11, Diamond Light Source using the "Oxford/Warwick Solid State Chemistry BAG to probe composition-structure–property relationships in solids" (CY32893). Neutron powder diffraction data were collected under RB2010395-1. This work used the Hamilton HPC service at Durham University. C. A. M. S., U. D. and N. C. B. acknowledge the Leverhulme Trust for a research project grant (grant no. RPG-2020-206). WTC acknowledges the National Science and Technology Council in Taiwan for funding 111-2112-M-002-044-MY3, 112-2124-M-002-012, and Academia Sinica project number AS-iMATE-113-12, and the Featured Areas Research Center Program within the framework of the Higher Education Sprout Project by the Ministry of Education in Taiwan 113L9008.

References

1 N. A. Hill, Why Are There so Few Magnetic Ferroelectrics?, *J. Phys. Chem. B*, 2000, **104**, 6694–6709.
2 R. E. Cohen, Origin of Ferroelectricity in Perovskite Oxides, *Nature*, 1992, **358**, 136–138.
3 J. Wang, J. B. Neaton, H. Zheng, V. Nagarajan, S. B. Ogale, B. Liu, D. Viehland, V. Vaithyanathan, D. G. Schlom, U. V. Waghmare, N. A. Spaldin, K. M. Rabe, M. Wuttig and R. Ramesh, Epitaxial $BiFeO_3$ Multiferroic Thin Film Heterostructures, *Science*, 2003, **299**, 1719–1722.
4 T. Kimura, S. Kawamoto, I. Yamada, M. Azuma, M. Takano and Y. Tokura, Magnetocapacitance Effect in Multiferroic $BiMnO_3$, *Phys. Rev. B: Condens. Matter Mater. Phys.*, 2003, **67**, 180401.
5 M. Kumar, S. Shankar, A. Kumar, A. Anshul, M. Jayasimhadri and O. P. Thakur, Progress in Multiferroic and Magnetoelectric Materials: Applications, Opportunities and Challenges, *J. Mater. Sci.: Mater. Electron.*, 2020, **31**, 19487–19510.
6 A. P. Levanyuk and D. G. Sannikov, Improper Ferroelectrics, *Sov. Phys. Uspekhi*, 1974, **17**, 199.
7 E. Bousquet, M. Dawber, N. Stucki, C. Lichtensteiger, P. Hermet, S. Gariglio, J.-M. Triscone and P. Ghosez, Improper Ferroelectricity in Perovskite Oxide Artificial Superlattices, *Nature*, 2008, **452**, 732–736.
8 N. A. Benedek and C. J. Fennie, Hybrid Improper Ferroelectricity: A Mechanism for Controllable Polarization-Magnetization Coupling, *Phys. Rev. Lett.*, 2011, **106**, 107204.
9 M. S. Senn and N. C. Bristowe, A Group-Theoretical Approach to Enumerating Magnetoelectric and Multiferroic Couplings in Perovskites, *Acta Crystallogr.*, 2018, **A74**, 308–321.
10 P. Toledano and J. C. Toledano, *The Landau Theory of Phase Transitions: Application to Structural, Incommensurate, Magnetic and Liquid Crystsal Systems*, World Scientific Publishing Company, 1987, vol. 3.
11 G. Kresse and J. Furthmüller, Efficiency of Ab-Initio Total Energy Calculations for Metals and Semiconductors Using a Plane-Wave Basis Set, *Comput. Mater. Sci.*, 1996, **6**, 15–50.
12 G. Kresse and J. Furthmüller, Efficient Iterative Schemes for Ab Initio Total-Energy Calculations Using a Plane-Wave Basis Set, *Phys. Rev. B: Condens. Matter Mater. Phys.*, 1996, **54**, 11169–11186.
13 G. Kresse and D. Joubert, From Ultrasoft Pseudopotentials to the Projector Augmented-Wave Method, *Phys. Rev. B: Condens. Matter Mater. Phys.*, 1999, **59**, 1758–1775.
14 J. P. Perdew, A. Ruzsinszky, G. I. Csonka, O. A. Vydrov, G. E. Scuseria, L. A. Constantin, X. Zhou and K. Burke, Restoring the Density-Gradient Expansion for Exchange in Solids and Surfaces, *Phys. Rev. Lett.*, 2008, **100**, 136406.
15 A. I. Liechtenstein, V. I. Anisimov and J. Zaanen, Density-Functional Theory and Strong Interactions: Orbital Ordering in Mott-Hubbard Insulators, *Phys. Rev. B: Condens. Matter Mater. Phys.*, 1995, **52**, R5467–R5470.
16 S. W. Jang, S. Ryee, H. Yoon and M. J. Han, Charge Density Functional plus U Theory of $LaMnO_3$: Phase Diagram,

Electronic Structure, and Magnetic Interaction, *Phys. Rev. B*, 2018, **98**, 125126.

17 M. M. Schmitt, Y. Zhang, A. Mercy and P. Ghosez, Electron-Lattice Interplay in $LaMnO_3$ from Canonical Jahn-Teller Distortion Notations, *Phys. Rev. B*, 2020, **101**, 214304.

18 S. Steiner, S. Khmelevskyi, M. Marsmann and G. Kresse, Calculation of the Magnetic Anisotropy with Projected-Augmented-Wave Methodology and the Case Study of Disordered $Fe_{1-x}Co_x$ Alloys, *Phys. Rev. B*, 2016, **93**, 224425.

19 D. Hobbs, G. Kresse and J. Hafner, Fully Unconstrained Noncollinear Magnetism within the Projector Augmented-Wave Method, *Phys. Rev. B: Condens. Matter Mater. Phys.*, 2000, **62**, 11556–11570.

20 B. J. Campbell, H. T. Stokes, D. E. Tanner and D. M. Hatch, ISODISPLACE: A Web-Based Tool for Exploring Structural Distortions, *J. Appl. Crystallogr.*, 2006, **39**, 607–614.

21 H. T. Stokes, D. M. Hatch and B. J. Campbell, *ISODISTORT, ISOTROPY Software Suite.* iso.byu.edu.

22 M. S. Senn, F. Orlandi, W. T. Chen, F. Pomiro and G. Clarke, New Perovskite $CeBaMn_2O_6$: A Potential Target System to Achieve Magnetoelectric Coupling, *STFC ISIS Neutron Muon Source*, 2020, DOI: 10.5286/ISIS.E.RB2010395.

23 L. C. Chapon, P. Manuel, P. G. Radaelli, C. Benson, L. Perrott, S. Ansell, N. J. Rhodes, D. Raspino, D. Duxbury, E. Spill and J. Norrs, Wish: The New Powder and Single Crystal Magnetic Diffractometer on the Second Target Station, *Neutron News*, 2011, **22**, 22–25.

24 J. S. O. Evans, Advanced Input Files & Parametric Quantitative Analysis Using Topas, *Mater. Sci. Forum*, 2010, **651**, 1–9.

25 G. King and P. M. Woodward, Cation Ordering in Perovskites, *J. Mater. Chem.*, 2010, **20**, 5785–5796.

26 G. Matsumoto, Study of $(La_{1-x}Ca_x)MnO_3$. I. Magnetic Structure of $LaMnO_3$, *J. Phys. Soc. Jpn.*, 1970, **29**, 606–615.

27 V. Skumryev, F. Ott, J. M. D. Coey, A. Anane, J.-P. Renard, L. Pinsard-Gaudart and A. Revcolevschi, Weak Ferromagnetism in $LaMnO_3$, *Eur. Phys. J. B*, 1999, **11**, 401–406.

28 A. T. Mulder, N. A. Benedek, J. M. Rondinelli and C. J. Fennie, Turning ABO3 Antiferroelectrics into Ferroelectrics: Design Rules for Practical Rotation-Driven Ferroelectricity in Double Perovskites and $A_3B_2O_7$ Ruddlesden-Popper Compounds, *Adv. Funct. Mater.*, 2013, **23**, 4810–4820.

29 P. Anderson, New Approach to the Theory of Superexchange Interactions, *Phys. Rev.*, 1959, **115**, 2–13.

30 J. B. Goodenough, Theory of the Role of Covalence in the Perovskite-Type Manganites $(La,M)MnO_3$, *Phys. Rev.*, 1955, **100**, 564.

31 J. Kanamori, Superexchange Interaction and Symmetry Properties of Electron Orbitals, *J. Phys. Chem. Solids*, 1959, **10**, 87–98.

32 T. Arima, Y. Tokura and J. B. Torrance, Variation of Optical Gaps in Perovskite-Type 3d Transition-Metal Oxides, *Phys. Rev. B: Condens. Matter Mater. Phys.*, 1993, **48**, 17006–17009.

33 J. P. Perdew, Density Functional Theory and the Band Gap Problem, *Int. J. Quantum Chem.*, 1985, **28**, 497–523.

34 R. D. King-Smith and D. Vanderbilt, Theory of Polarization of Crystalline Solids, *Phys. Rev. B: Condens. Matter Mater. Phys.*, 1993, **47**, 1651–1654.

35 C. J. Fennie and K. M. Rabe, Ferroelectric Transition in $YMnO_3$ from First Principles, *Phys. Rev. B: Condens. Matter Mater. Phys.*, 2005, **72**, 100103.

36 T. Nakajima, H. Kageyama, H. Yoshizawa and Y. Ueda, Structures and Electromagnetic Properties of New Metal-Ordered Manganites: $RBaMn_2O_6$ (R = Y and Rare-Earth Elements), *J. Phys. Soc. Jpn.*, 2002, **71**, 2843–2846.

37 E. Solana-Madruga, Á. M. Arévalo-López, A. J. Dos Santos-García, E. Urones-Garrote, D. Ávila-Brande, R. Sáez-Puche and J. P. Attfield, Double Double Cation Order in the High-Pressure Perovskites $MnRMnSbO_6$, *Angew. Chem., Int. Ed.*, 2016, **55**, 9340–9344.

38 E. Solana-Madruga, A. J. D. santos-García, A. M. Arévalo-López, D. Ávila-Brande, C. Ritter, J. P. Attfield and R. Sáez-Puche, High Pressure Synthesis of Polar and Non-Polar Cation-Ordered Polymorphs of Mn_2ScSbO_6, *Dalton Trans.*, 2015, **44**, 20441–20448.

39 A. A. Belik, D. D. Khalyavin, Y. Matsushita and K. Yamaura, Triple A-Site Cation Ordering in the Ferrimagnetic $Y_2CuGaMn_4O_{12}$ Perovskite, *Inorg. Chem.*, 2022, **61**, 14428–14435.

40 S. V. Trukhanov, I. O. Troyanchuk, M. Hervieu, H. Szymczak and K. Bärner, Magnetic and Electrical Properties of $LBaMn_2O_{6-\gamma}$ (L = Pr, Nd, Sm, Eu, Gd, Tb) Manganites, *Phys. Rev. B: Condens. Matter Mater. Phys.*, 2002, **66**, 184424.

41 T. Nakajima, H. Yoshizawa and Y. Ueda, A-Site Randomness Effect on Structural and Physical Properties of Ba-Based Perovskite Manganites, *J. Phys. Soc. Jpn.*, 2004, **73**, 2283–2291.

42 Y. Ueda and T. Nakajima, Novel Structures and Electromagnetic Properties of the A-Site-Ordered/Disordered Manganites $RBaMn_2O_6/R_{0.5}Ba_{0.5}MnO_3$ (R = Y and Rare Earth Elements), *J. Phys.: Condens. Matter*, 2004, **16**, S573.

43 G. Liu, Q. Lei, M. A. Wolak, Q. Li, L.-Q. Chen, C. Winkler, J. Sloppy, M. L. Taheri and X. Xi, Epitaxial Strain and Its Relaxation at the $LaAlO_3/SrTiO_3$ Interface, *J. Appl. Phys.*, 2016, **120**, 085302.

44 D. I. Woodward and I. M. Reaney, Electron Diffraction of Tilted Perovskites, *Acta Crystallogr.*, 2005, **B61**, 387–399.

45 I. M. Reaney, E. L. Colla and N. Setter, Dielectric and Structural Characteristics of Ba- and Sr-Based Complex Perovskites as a Function of Tolerance Factor, *Jpn. J. Appl. Phys.*, 1994, **33**, 3984–3990.

46 C. J. Howard, K. S. Knight, B. J. Kennedy and E. H. Kisi, Structural Phase Transitions in Strontium Zirconate Revisited, *J. Phys.: Condens. Matter*, 2000, **12**, L677.

47 K. Kishida, K. Goto and H. Inui, Electron Diffraction of ABX_3 Perovskites with Both Layered Ordering of A Cations and Tilting of BX_6 Octahedra, *Acta Crystallogr.*, 2009, **B65**, 405–415.

48 K. F. Wang, Y. Wang, L. F. Wang, S. Dong, D. Li, Z. D. Zhang, H. Yu, Q. C. Li and J.-M. Liu, Cluster-Glass State in Manganites Induced by A-Site Cation-Size Disorder, *Phys. Rev. B: Condens. Matter Mater. Phys.*, 2006, **73**, 134411.

49 C.-M. Chin, P. D. Battle, A. L. Goodwin and A. Wildes, Short-Range Cation and Spin Ordering in the Relaxor Ferromagnet $La_3Ni_2SbO_9$ Studied by Polarized-Neutron Scattering and Monte-Carlo Methods, *J. Solid State Chem.*, 2019, **278**, 120920.

50 P. Kearins, E. Solana-Madruga, K. Ji, C. Ritter and J. P. Attfield, Cluster Spin Glass Formation in the Double Double Perovskite $CaMnFeTaO_6$, *J. Phys. Chem. C*, 2021, **125**, 9550–9555.

51 D. Akahoshi, M. Uchida, Y. Tomioka, T. Arima, Y. Matsui and Y. Tokura, Random Potential Effect near the Bicritical Region in Perovskite Manganites as Revealed by Comparison with the Ordered Perovskite Analogs, *Phys. Rev. Lett.*, 2003, **90**, 177203.

52 J. Blasco, G. Subías, M. L. Sanjuán, J. L. García-Muñoz, F. Fauth and J. García, Structure and Phase Transitions in A-Site Ordered $RBaMn_2O_6$ (R = Pr, Nd) Perovskites with a Polar Ground State, *Phys. Rev. B*, 2021, **103**, 064105.

53 C. A. Randall and A. S. Bhalla, Nanostructural–Property Relations in Complex Lead Perovskites, *Jpn. J. Appl. Phys.*, 1990, **29**, 327.

54 A. Kumar, J. N. Baker, P. C. Bowes, M. J. Cabral, S. Zhang, E. C. Dickey, D. L. Irving and J. M. LeBeau, Atomic-Resolution Electron Microscopy of Nanoscale Local Structure in Lead-Based Relaxor Ferroelectrics, *Nat. Mater.*, 2021, **20**, 62–67.

55 L. M. Daniels, R. J. Kashtiban, D. Kepaptsoglou, Q. M. Ramasse, J. Sloan and R. I. Walton, Local A-Site Layering in Rare-Earth Orthochromite Perovskites by Solution Synthesis, *Chem. – Eur. J.*, 2016, **22**, 18362–18367.